Chinese Journal of Natural Medicines

Diketopiperazines with anti-skin inflammation from marine-derived endophytic fungus *Aspergillus* sp. and configurational reassignment of aspertryptanthrins

Jin Yang, Xianmei Xiong, Lizhi Gong, Fengyu Gan, Hanling Shi, Bin Zhu, Haizhen Wu, Xiujuan Xin, Lingyi Kong, Faliang An

Citation: Jin Yang, Xianmei Xiong, Lizhi Gong, Fengyu Gan, Hanling Shi, Bin Zhu, Haizhen Wu, Xiujuan Xin, Lingyi Kong, Faliang An, Diketopiperazines with anti-skin inflammation from marine-derived endophytic fungus *Aspergillus* sp. and configurational reassignment of aspertryptanthrins, Chinese Journal of Natural Medicines, 2025, 23(8), 980-989. doi: 10.1016/S1875-5364(25)60933-2.

View online: https://doi.org/10.1016/S1875-5364(25)60933-2

Chinese Journal of Natural Medicines 23 (2025) 980-989

Contents lists available at ScienceDirect

Chinese Journal of Natural Medicines

journal homepage: www.cjnmcpu.com/

Original article

Diketopiperazines with anti-skin inflammation from marine-derived endophytic fungus *Aspergillus* sp. and configurational reassignment of aspertryptanthrins

Jin Yang[a,Δ], Xianmei Xiong[a,Δ], Lizhi Gong[a], Fengyu Gan[a], Hanling Shi[a], Bin Zhu[a], Haizhen Wu[a], Xiujuan Xin[a], Lingyi Kong[b], Faliang An[a,c,*]

[a] *State Key Laboratory of Bioreactor Engineering, East China University of Science and Technology, Shanghai 200237, China*
[b] *Jiangsu Key Laboratory of Bioactive Natural Product Research and State Key Laboratory of Natural Medicines, School of Traditional Chinese Pharmacy, China Pharmaceutical University, Nanjing 210009, China*
[c] *Marine Biomedical Science and Technology Innovation Platform of Lin-gang Special Area, Shanghai 201306, China*

ARTICLE INFO

Article history:
Received 6 November 2024
Revised 21 January 2025
Accepted 7 March 2025
Available online 20 August 2025

Keywords:
Diketopiperazines
Aspergillus sp.
Configurational reassignment
Anti-skin inflammation

ABSTRACT

Two novel diketopiperazines (**1** and **5**), along with ten known compounds (**2**–**4**, **6**–**12**) demonstrating significant skin inflammation inhibition, were isolated from a marine-derived fungus identified as *Aspergillus* sp. FAZW0001. The structural elucidation and configurational reassessments of compounds **1**–**5** were established through comprehensive spectral analyses, with their absolute configurations determined *via* single crystal X-ray diffraction using Cu K*α* radiation, Marfey's method, and comparison between experimental and calculated electronic circular dichroism (ECD) spectra. Compounds **1**, **2**, and **8** exhibited significant anti-inflammatory activities in *Propionibacterium acnes* (*P. acnes*)-induced human monocyte cell lines. Compound **8** demonstrated the ability to down-regulate interleukin-1β (IL-1β) expression by inhibiting Toll-like receptor 2 (TLR2) expression and modulating the activation of myeloid differentiation factor 88 (MyD88), mitogen-activated protein kinase (MAPK), and nuclear factor *κ*B (NF-*κ*B) signaling pathways, thus reducing the cellular inflammatory response induced by *P. acnes*. Additionally, compound **8** showed the capacity to suppress mitochondrial reactive oxygen species (ROS) production and nucleotide-binding oligomerization domain-like receptor protein 3 (NLRP3) inflammasome activation, thereby reducing IL-1β maturation and secretion. A three-dimensional quantitative structure-activity relationships (3D-QSAR) model was applied to compounds **5**–**12** to analyze their anti-inflammatory structure-activity relationships.

1. Introduction

Acne vulgaris, a widespread skin condition affecting individuals across all age groups, affects approximately 90% of males and 80% of females aged between 13 and 17 [1]. This prevalent skin condition manifests throughout the body, particularly on the face. Its adverse impact on appearance can trigger significant psychological distress, potentially leading to reduced self-esteem, feelings of inadequacy, and depression, resulting in both physical and psychological consequences [2].

The pathogenesis of acne begins with sebaceous gland hyperactivity, hair follicle hyperkeratosis, and immunological changes conducive to bacterial colonization and inflammation, particularly by acne Bacteroides [3]. In acne development, *Propionibacterium acnes* (*P. acnes*) mediates changes in various intracellular signaling pathways *via* Toll-like receptor 2 (TLR2) on the cell membrane, significantly influencing acne-related inflammation. Beyond TLR activation, *P. acnes* stimulates NLRs, essential inflammasome genes that trigger inflammatory and anti-microbial responses [4]. Nucleotide-binding oligomerization domain-like receptor protein 3 (NLRP3) inflammasome activation induces cell death and inflammation, releasing cellular contents and intensifying inflammatory responses [5]. Contemporary acne treatments and pharmaceuticals present certain adverse effects, necessitating the development of novel anti-acne therapeutics [6]. Natural product-based drugs typically demonstrate strong biocompatibility and considerable potential for chemical structural modification. These natural compounds effectively interact with biological targets and demonstrate significant biological activity [7].

In our ongoing investigation of chemically novel and biologically active compounds [8-11], two new diketopiperazines (**1** and **5**) featuring unusual oxidized ring systems, along with ten known related compounds (**2**–**4**, **6**–**12**), were isolated and characterized from a marine-derived endophytic fungi *Aspergillus* sp. FAZW-0001 (Fig. 1). Aspertryptanthrins C–D (**1**–**2**) feature a rare 16-membered phenylate ring framework, while gartryprostatin D (**5**) contains a rare 6/6/5/5/5/6/5 seven-ring diketopiperazine skeleton, incorporating an additional fused tetrahydrofuran ring

* Corresponding author.
E-mail address: flan2016@ecust.edu.cn
Δ These authors contributed equally to this work.

https://doi.org/10.1016/S1875-5364(25)60933-2

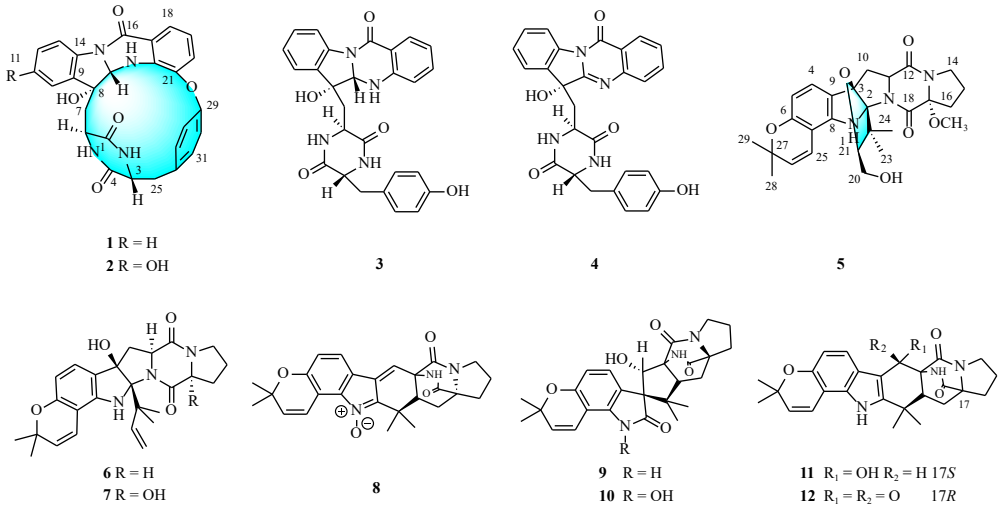

1 R = H
2 R = OH
3
4
5
6 R = H
7 R = OH
8
9 R = H
10 R = OH
11 R_1 = OH R_2 = H 17*S*
12 R_1 = R_2 = O 17*R*

Fig. 1 Chemical structures of compounds **1**–**12**.

at C-2 and C-3. The distinctive 16-membered ring framework and (epoxyethano)pyrrolo[2, 3-b]pyrrole skeleton were conclusively determined through single crystal X-ray diffraction using Cu K*α* radiation, providing definitive results superior to chemical, spectroscopic, and computational methods. Configuration assignment for these multicyclic alkaloids represents a crucial step in structural determination. The essential stereo-configurations of C-3 and C-8 in aspertryptanthrins A–C were revised using single-crystal X-ray diffraction with Cu K*α* radiation and Marfey's method. In bioassays, compounds **1**, **2**, **8**, **9**, and **11** demonstrated significant anti-inflammatory activity on *P. acnes*-induced human monocyte cell lines (THP-1). This paper presents the isolation, structural elucidation, anti-inflammatory assessment, three-dimensional quantitative structure-activity relationships (3D-QSAR) of isolates, and the potential acne therapeutic mechanism of **8** on THP-1 cells.

2. Results and discussion

2.1. Structural identification of isolated compounds

Compound **1** crystallized as a block crystal. Its molecular formula, $C_{27}H_{22}N_4O_5$, was established through high-resolution electrospray ionization mass spectrometry (HR-ESI-MS) analysis, which displayed an ion peak $[M + H]^+$ at *m/z* 483.1659 (Calcd. for $C_{27}H_{23}N_4O_5$, 483.1663). The ^{13}C nuclear magnetic resonance (NMR) data (Table 1) confirmed this molecular formula. The ^1H NMR spectrum revealed one ortho-disubstituted aromatic ring [δ_H 7.37 (dd, *J* = 7.9, 1.2 Hz, H-10), 7.14 (t, *J* = 7.9 Hz, H-11), 7.40 (t, *J* = 7.9 Hz, H-12), 8.00 (d, *J* = 7.9 Hz, H-13)], one para-disubstituted aromatic ring [δ_H 7.19 (dd, *J* = 8.3, 2.2 Hz, H-27), 7.30 (dd, *J* = 8.3, 2.7 Hz, H-28), 6.66 (dd, *J* = 8.4, 2.7 Hz, H-30), 7.05 (dd, *J* = 8.4, 2.2 Hz, H-31)], and one tri-substituted aromatic ring [δ_H 7.78 (dd, *J* = 7.8, 1.4 Hz, H-18), 7.17 (t, *J* = 7.8 Hz, H-19), 7.51 (dd, *J* = 7.8, 1.4 Hz, H-20), 7.05 (dd, *J* = 8.4, 2.2 Hz, H-31)]. A comprehensive analysis of the NMR data (Table 1) indicated that **1** was a structural analog of aspertryptanthrin C (**2**). The primary difference was the presence of a tryptophan residue in **1** instead of a hydroxylated tryptophan residue in **2**, corresponding to a 16-unit difference in HR-ESI-MS data. This structural assignment was supported by key correlations in the ^1H–^1H correlation spectroscopy (COSY) spectrum between H-10/H-11/H-12/H-13 and in the heteronuclear multiple bond correlation (HMBC) spectrum from H-11 to C-9 and C-13 (Fig. 2A). The phenylate bridge between C-21 and C-29 was confirmed by the correlation between NH-23 and H-28 in the rotating-frame Overhauser effect spectroscopy (ROESY) spectrum (Fig. 2B). Therefore, **1** was identified as 11-dehydroxylated aspertryptanthrin C and designated as aspertryptanthrin D. The ROESY correlations between H-24 and H-7b, and between H-24 and H-6 indicated spatial proximity of these protons, which differed from the reported assignment in **2**. Single-crystal X-ray diffraction analysis using Cu K*α* radiation [Flack parameter value of 0.10 (12)] definitively established the relative and absolute configurations of **1**. To resolve the discrepancies between compounds **1** and **2**, their 1D, 2D NMR, and electronic circular dichroism (ECD) data were systematically analyzed and compared in subsequent discussions.

The molecular formula of **2** was established as $C_{27}H_{22}N_4O_6$, confirmed by HR-ESI-MS analysis showing an ion peak $[M + H]^+$ at *m/z* 499.1608 (Calcd. for $C_{27}H_{23}N_4O_6$, 499.1612). Analysis of the ^1H and ^{13}C NMR spectra in DMSO-d_6 solvent confirmed that the planar structure of **2** corresponded to aspertryptanthrin C. The ROESY spectrum revealed correlations between H-24 and H-7b, and between H-24 and H-6, indicating *β*-orientation (Fig. 2B). The absolute configurations at C-8 and C-24 in aspertryptanthrin C were previously determined using a combination of the negative cotton effect around 350 nm in $Rh_2(OCOCF_3)_4$-induced ECD spectrum and comparison of calculated and experimental ECD spectra. The absolute configurations at C-3 and C-6 of the compound were initially misassigned as *S*,*S* due to the overlooked influence of fungal amino acid isomerization enzymes, which can modify stereochemistry during biosynthesis (Fig. 3). To resolve this, single-crystal X-ray diffraction —recognized as the most definitive method for stereochemical determination —was employed. Crystals suitable for analysis were obtained by recrystallization from a variety of solvent systems to ensure accurate structural elucidation. Successfully, **2** crystallized from a MeOH–H_2O mixture (95∶5). Single-crystal X-ray diffraction experiments using Cu K*α* radiation (Flack parameter value of 0.30) definitively established the relative configurations of **2**. The experimental ECD spectrum of **1** exhibited close similarity to that of **2**. Subsequently, the absolute configurations of both **1** and **2** were determined as 3*R*,6*S*,8*R*,24*S* (Fig. 4A).

Compounds **3** and **4** were characterized as aspertryptanthrins A and B through HR-ESI-MS data and detailed analysis of ^1H and ^{13}C NMR spectra. These findings necessitated an investigation into the absolute configurations of C-3 in aspertryptanthrins A and B. Amino acid analysis of the **4** hydrolysate using Marfey's method revealed the *R* configuration of C-3 (D-Tyr) (Fig. S30), further confirmed by single-crystal X-ray diffraction experiments of **3** and **4** with Cu K*α* radiation (Fig. S31 and Fig. 4B). This indicated that the previously assigned absolute configurations of C-3 in **3** and **4** were incorrect. Moreover, the absolute configuration

Table 1 ^{1}H (600 MHz) and ^{13}C (150 MHz) NMR data for compounds **1** and **5** (**1** in DMSO-d_6, **5** in $CDCl_3$).

No.	1		No.	5	
	δ_C	δ_H (m; *J* in Hz)		δ_C	δ_H (m; *J* in Hz)
1	168.8		1(NH)		
2(NH)		8.36 (d, 3.2)	2	98.6	
3	57.1	4.12 (m)	3	97.1	
4	168.1		4	125.2	6.97 (d, 8.1)
5(NH)		7.12 (s)	5	108.0	6.20 (d, 8.1)
6	49.8	2.40 (dd, 6.5, 2.2)	6	155.1	
7	41.7	a 2.35 (dd, 2.3, 15.0)	7	103.7	
		b 2.14 (dd, 6.5, 15.0)			
8	76.1		8	146.8	
9	134.9		9	118.8	
10	130.5	7.37 (dd, 1.2, 7.9)	10	38.9	a 2.72 (dd, 12.9, 7.0)
					b 2.59 (m)
11	124.6	7.14 (t, 7.9)	11	63.4	4.59 (dd, 11.9, 7.0)
12	124.6	7.40 (t, 7.9)	12	167.1	
13	115.1	8.00 (d, 7.9)			
14	139.8		14	45.3	3.56 (m)
			15	21.0	a 1.99 (m), b 1.90 (m)
16	159.4		16	31.6	a 2.33 (m), b 2.10 (m)
17	124.2		17	93.6	
18	124.6	7.78 (dd, 1.4, 7.8)	18	165.4	
19	122.2	7.17 (t, 7.8)	19		
20	126.6	7.51 (dd, 1.4, 7.8)	20	61.8	a 3.64 (m), b 3.56 (m)
21	145.7		21	91.1	3.81 (dd, 7.6, 2.8)
22	137.7		22	46.7	
23(NH)		4.41 (d, 7.2)	23	21.2	1.29 (s)
24	75.3	4.69 (d, 7.2)	24	18.2	0.82 (s)
25	39.6	a 3.16 (dd, 3.0, 13.3)	25	116.6	6.15 (d, 9.9)
		b 2.82 (dd, 4.3, 13.3)			
26	130.1		26	129.1	5.50 (d, 9.9)
27	132.0	7.19 (dd, 2.2, 8.3)	27	76.0	
28	118.8	7.30 (dd, 2.7, 8.3)	28	28.2	1.37 (s)
29	157.8		29	27.6	1.35 (s)
30	115.0	6.66 (dd, 2.7, 8.4)	17-OMe	52.1	3.14 (s)
31	132.3	7.05 (dd, 2.2, 8.4)			
8-OH		6.42 (s)			

of C-8 in **4** differed from that of **1**–**3**. To resolve this discrepancy, a high-quality crystal of **4** was successfully cultivated after multiple attempts, enabling the stereochemical configuration correction of C-8. Consequently, the absolute configurations of **3** and **4** were conclusively determined and revised, as shown in Fig. 3.

Compound **5** was obtained as a block crystal, with its molecular formula determined as $C_{27}H_{33}N_3O_6$ by HR-ESI-MS, exhibiting an $[M + Na]^+$ ion peak at *m/z* 518.2263 (Calcd. for $C_{27}H_{33}N_3O_6Na$, 518.2262), indicating 13 degrees of unsaturation. Analysis of the ^{1}H, ^{13}C NMR, and HSQC spectra (Figs. S17–S20) revealed the presence of five methyl groups (including one oxygen-bearing methyl), five sp^3-methylenes (including one oxygen-bearing methylene), two sp^3-methine carbon signals (including one oxygenated carbon), five sp^3 non-protonated carbons (including three oxygen-bearing carbons), four olefinic methines, and six sp^2 non-protonated carbons. Upon comparison with previously reported data, the signals in the ^{1}H and ^{13}C NMR spectra of **5** closely resembled those of gartryprostatin B [12], with the addition of a methoxy group (δ_H 3.14; δ_C 52.1). Therefore, **5** was initially identified as 17-methoxylated gartryprostatin A, displaying a rare 6/6/5/5/6/5/5 seven-ring framework among prenylated indole diketopiperazines. Further investigation of similar diketopiperazines from this strain's secondary metabolites led to the isolation of two potential precursor molecules of **5**: notoamide D (**6**) and 17-hydroxynotoamide D (**7**). To confirm the planar structure of **5**, determining the hydroxyl group position was essential. However, the hydroxyl group signal remained undetectable in the NMR spectrum using either $CDCl_3$ or DMSO-d_6 as solvents. This raised questions about the rare seven-ring framework, particularly without X-ray diffraction data for gartryprostatins A and B. X-ray diffraction analysis was determined to be the optimal method for structure verification. After multiple crystallization attempts, a suitable crystal was obtained in MeOH–CH_2Cl_2–H_2O (10∶1∶1) at 15 °C and analyzed using Cu Kα radiation [Flack parameter value of −0.07 (8)]. This analysis confirmed both the planar structure and absolute configuration as 2*S*,3*R*,11*S*,17*R*,21*S*. Based on these comprehensive analyses, **5** was definitively identified as 17-methoxylated gartryprostatin A, featuring an unusual septenary cyclic ring system.

Compounds **2**–**4** and **6**–**12** were identified as aspertryptanthrin C (**2**) [13], aspertryptanthrin A (**3**) [13], aspertryptanthrin B (**4**) [13], notoamide D (**6**) [14], 17-hydroxynotoamide D (**7**) [15], asperthrin A (**8**) [11], sclerotiamide (**9**) [16], notoamide H (**10**) [17], notoamide R (**11**) [18], (−)-notoamide I (**12**) [19], respectively, through comparison with published NMR data. All isolated compounds (**1**–**12**) were evaluated for their inhibitory effects on skin inflammation in *P. acnes* induced THP-1. Compounds **1**, **2**, **8**, **9** and **11** demonstrated significant anti-inflammatory activity with half maximal inhibitory concentration (IC_{50}) values of 37.6 ± 1.23, 45.8 ± 3.17, 1.12 ± 0.41, 27.68 ± 4.17, and 19.56 ± 3.63 μmol·L^{-1}, respectively.

*2.2. Exploring the anti-inflammatory mechanism of compound **8***

Variations in cellular viability can significantly affect the accuracy of anti-inflammatory screening. This study aimed to determine a safe concentration range where the compound **8** does not significantly impact cell viability in THP-1 cells using the methyl thiazolyl tetrazolium (MTT) method. The results established a safe concentration range for **8** of 0–3.0 μmol·L^{-1} (Fig. S32A). The identical methodology was applied to establish the safe concentration range of the positive drug, tretinoin, which was determined to be 0–10 μmol·L^{-1}. Subsequently, concentrations of 0.75, 1.5, and 3.0 μmol·L^{-1} were selected for anti-inflammatory assays. The secretion of inflammatory mediators by cells depends on the quantity and viability of *P. acnes*. To ensure that anti-inflammatory effects were not attributable to *P. acnes* inhibition, it was essential to assess the anti-*P. acnes* activity of **8**. The minimum inhibitory concentration (MIC) of **8** against *P. acnes* was established at 250 μmol·L^{-1} using the micro-broth method. Therefore, the concentration range of 0–3.0 μmol·L^{-1} for **8** demonstrated no effect on *P. acnes*.

Interleukin-1β (IL-1β), when activated, functions as a potent proinflammatory cytokine essential for initiating and enhancing inflammation. This process occurs through the recruitment of innate immune cells and inducing IL-6 production [20]. Additionally,

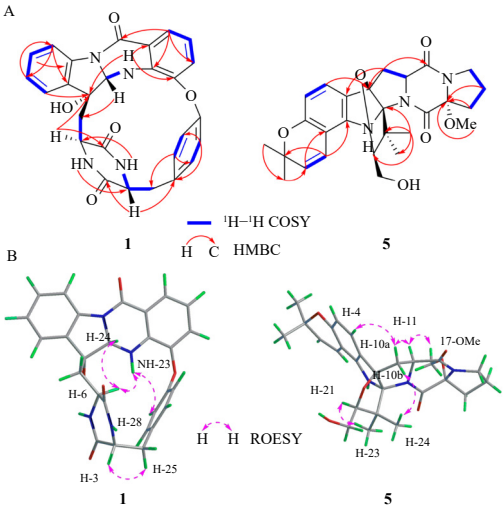

Fig. 2 (A) ^{1}H–^{1}H COSY, key HMBC correlations of **1** and **5**. (B) Key ROESY correlations of **1** and **5**.

multiple inflammatory pathways contribute to regulating inflammatory responses, resulting in the production of various inflammatory mediators [21]. To examine inhibitory effects on inflammation, IL-1β messenger ribonucleic acid (mRNA) expression levels were evaluated *via* quantitative real-time polymerase chain reaction (qRT-PCR) (Fig. S32B). The model group exhibited elevated IL-1β mRNA expression in *P. acnes*-stimulated THP-1 cells, along with increased secretion levels of IL-1β, IL-6, IL-8, and tumor necrosis factor α (TNF-α). The secretion levels of IL-1β, IL-6, IL-8, and TNF-α (Fig. S32C–S32F) were measured using enzyme-linked immunosorbent assay (ELISA). Notably, Compound **8** significantly inhibited IL-1β mRNA expression and the secretion of inflammatory mediators IL-1β with the IC_{50} value 1.12 μmol·L^{-1}, exceeding tretinoin (IC_{50} 5.54 μmol·L^{-1}), highlighting its potential as a skincare anti-inflammatory agent.

Multiple studies have consistently demonstrated the crucial role of the TLR2 signaling pathway in the immune response triggered by *P. acnes* [22,23]. Previous research has demonstrated increased TLR2 expression in acne lesions, particularly near hair follicles. Moreover, the number of TLR2-containing cells was found to increase with acne lesion duration [24]. Enhanced TLR2 mRNA expression (Fig. 5B) and protein levels (Fig. 5C) were observed in THP-1 cells following *P. acnes* stimulation, accompanied by increased TLR2 distribution on the cell surface. However, treatment with **8** significantly reduced these effects, as shown in Fig. 5. When TLR2 on immune cell surfaces recognizes specific ligands on pathogenic microorganisms, it activates the myeloid differentiation factor 88 (MyD88)-IL-1 receptor-associated kinase 1 (IRAK1)-TNF receptor-associated factor 6 (TRAF6) kinase pathway for signal transduction [25]. *P. acnes* stimulation induced increased expression of MyD88, IRAK1, and TRAF6 proteins (Fig. 5C) in THP-1 cells, indicating MyD88-dependent pathway activation. However, MyD88, IRAK1, and TRAF6 expression levels decreased after treatment with **8** for 4 h, particularly at 3 μmol·L^{-1} (Figs. 5E and 5F). This indicated that **8** could inhibit MyD88-dependent pathway activation induced by *P. acnes* stimulation in THP-1 cells.

To elucidate the influence of TLR2 on IL-1β secretion, the TLR2 inhibitor C29 was employed in the experimental protocol. The results demonstrated that C29 significantly inhibited TLR2 protein expression (Fig. 5E) and suppressed the *P. acnes*-induced elevation in IL-1β transcription (Fig. 5D) and secretion levels. The combination of **8** and C29 exhibited enhanced inhibitory effects. Moreover, **8** suppressed IL-1β transcription through TLR2 expression inhibition, consequently reducing IL-1β secretion. C29 was additionally utilized to examine the relationship between TLR2 and the MyD88-dependent pathway. The findings revealed that C29 effectively suppressed the protein expression of MyD88, IRAK1, and TRAF6 (Figs. 5E and 5F) following *P. acnes* stimulation. These observations indicated that IL-1β secretion and MyD88-dependent pathway activation by *P. acnes* were dependent on TLR2 expression and mediation. Furthermore, **8**'s inhibitory effects on the MyD88-dependent pathway correlated with its TLR2 inhibition capacity. Thus, the data suggested that **8** modulated the *P. acnes*-induced immune response by targeting TLR2, thereby inhibiting the MyD88-dependent pathway.

During inflammatory responses, antigen-induced cellular activation initiates the mitogen-activated protein kinase (MAPK) signal transduction pathway [26]. The present study demonstrated that *P. acnes* stimulation of THP-1 cells increased the phosphorylation levels of p38, extracellular signal-regulated kinase (ERK), and c-Jun *N*-terminal kinase (JNK) proteins (Fig. S33A), indicating MAPK signaling pathway activation. Compound **8** demonstrated dose-dependent inhibition of protein phosphorylation, suggesting effective attenuation of *P. acnes*-induced MAPK signaling pathway activation in THP-1 cells.

To investigate the relationship between TLR2 and MAPK signaling pathways, experiments utilizing the TLR2 inhibitor C29 were conducted. The results demonstrated that C29 significantly reduced the phosphorylation of p38, ERK, and JNK proteins (Fig. S33B) induced by *P. acnes* stimulation. These observations sug-

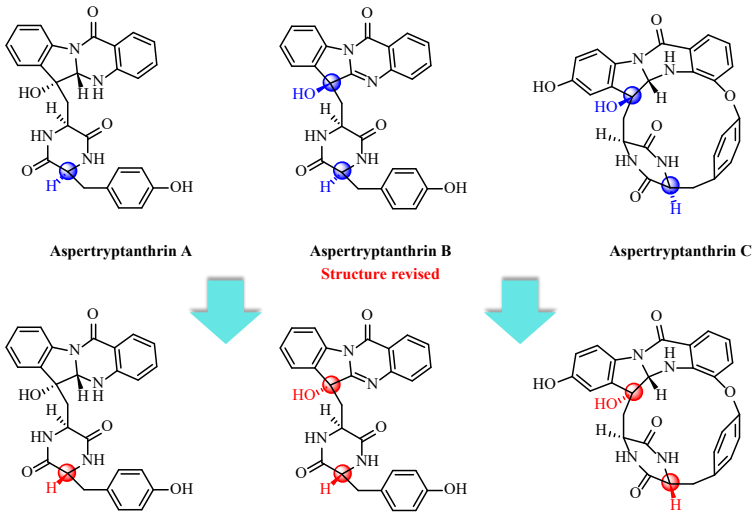

Fig. 3 Structural revision of aspertryptanthrins A–C (**2**–**4**).

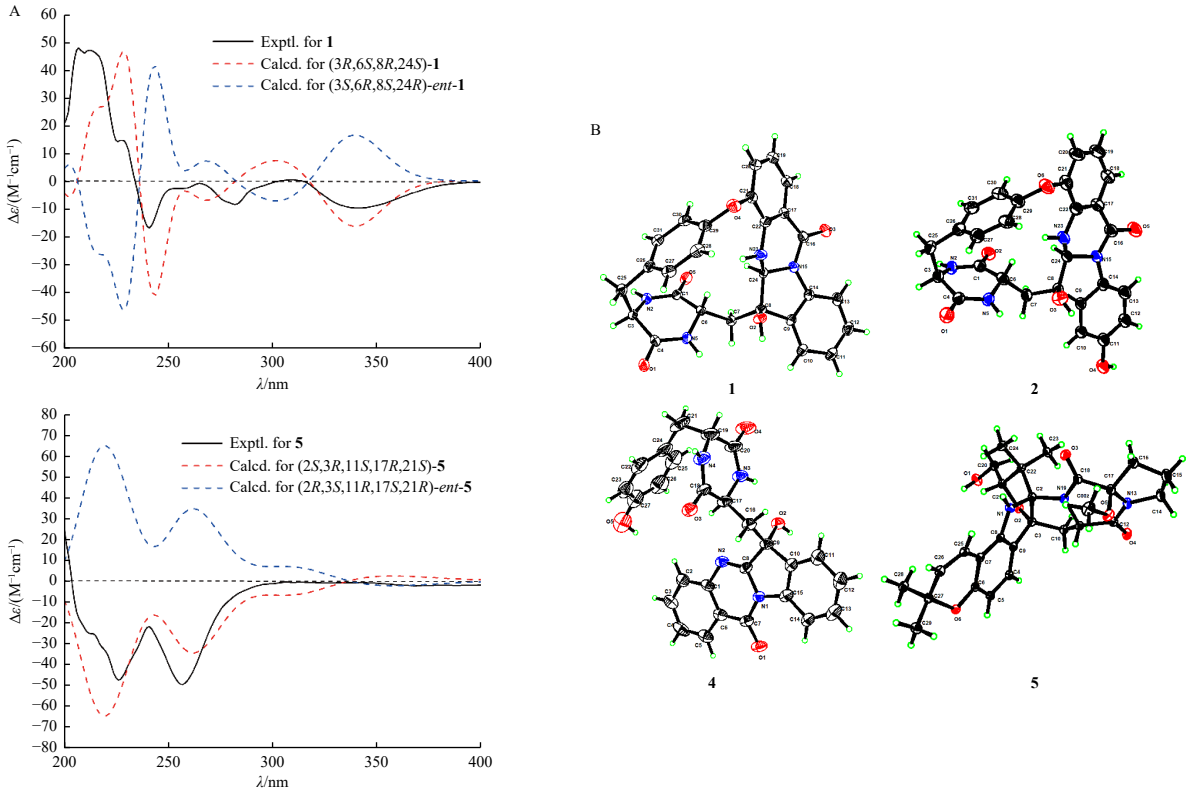

Fig. 4 (A) Experimental and calculated ECD spectra of **1** and **5**. (B) X-ray crystal structures of **1**, **2** and **4**, **5**.

gested that MAPK signaling pathway activation by *P. acnes* required TLR2 mediation. Additionally, the inhibitory effect of **8** on MAPK signaling pathways correlated with its TLR2 inhibition capacity. These findings confirmed TLR2's role in MAPK signaling pathway activation and established **8**'s mechanism of pathway inhibition through TLR2 suppression.

In quiescent THP-1 cells, the nuclear factor κB (NF-κB) and inhibitor of NF-κB (IκB) proteins form a complex in the cytoplasm. Upon stimulation by pathogenic bacteria, IκB within the complex undergoes phosphorylation, exposing the nuclear localization site of NF-κB. Subsequently, the IκB subunit undergoes ubiquitination and protease degradation, resulting in the release and phosphorylation of the NF-κB dimer (comprising p65 and p50 subunits) [27]. *P. acnes* stimulation of THP-1 cells induced enhanced phosphorylation of IκBα and total p65 proteins (Fig. S33C). Furthermore, decreased cytoplasmic levels and increased nuclear levels of phosphorylated p65 were observed (Figs. S33C and S33E), indicating NF-κB signaling pathway activation. Treatment with **8** at various concentrations decreased the expression of phosphorylated IκBα and total phosphorylated p65 proteins, while inhibiting nuclear translocation of phosphorylated p65. These results demonstrate that **8** inhibits the activation of the NF-κB signaling pathway induced by *P. acnes* stimulation in THP-1 cells in a dose-dependent manner.

TLR2-mediated nuclear translocation of NF-κB induces the upregulation of NLRP3 and pro-IL-1β expression, representing the initial phase of NLRP3 inflammasome activation, although it does not affect pro-caspase 1 and ASC expression [28]. This suggests that *P. acnes* stimulation may increase NLRP3 and pro-IL-1β expression, which **8** potentially inhibits. To examine this hypothesis, immunofluorescence analysis was conducted to measure intracellular NLRP3 levels. Fig. 6 shows NLRP3 protein labeled with green fluorescence and nuclei stained with blue fluorescence. Unstimulated THP-1 cells displayed minimal green fluorescence, indicating low NLRP3 protein levels. Following *P. acnes* exposure, green fluorescence intensity increased significantly, demonstrating enhanced NLRP3 protein expression (Fig. 6A). Treatment with increasing concentrations of **8** led to a dose-dependent decrease in intracellular green fluorescence, reflecting reduced NLRP3 protein expression (Figs. 6B and 6C). These preliminary findings indicate that **8** inhibits the upregulation of NLRP3 protein induced by *P. acnes* stimulation.

The maturation and secretion of IL-1β are regulated by the activation of NLRP3 inflammasomes through initiation and assembly processes [29]. To investigate the effect of inflammasome assembly on IL-1β maturation and secretion, studies using the NLRP3 inflammasome activation inhibitor MCC950 were performed. The findings revealed that MCC950 did not affect the increase in NLRP3 protein expression induced by *P. acnes* stimulation (Fig. 6D), suggesting that MCC950 did not inhibit the initiation phase of NLRP3 inflammasomes. However, MCC950 decreased the protein expressions of caspase 1 p20/pro-caspase 1 and IL-1β/pro-IL-1β, while reducing IL-1β secretion levels (Figs. 6B and 6D). These results demonstrated that IL-1β maturation and secretion were regulated by inflammasome assembly. Additionally, these findings indicated that **8** could suppress IL-1β maturation and secretion by inhibiting inflammasome assembly and blocking NLRP3 inflammasome activation.

Mitochondrial reactive oxygen species (mtROS), known to activate inflammasome assembly, serve a crucial function in the innate immune response to cellular and pathological injuries [30]. To examine the effect of **8** on mtROS release in pretreated THP-1 cells, a fluorescence probe method was utilized to evaluate the potential of **8** in suppressing NLRP3 inflammasome activation through targeting inflammasome assembly. After bacterial stimulation, an increase in mtROS was detected, evidenced by enhanced fluorescence intensity (red peak). However, with the introduction of varying concentrations of **8**, the fluorescence intensity shift decreased (yielding purple, blue, and green peaks) (Fig. 7A). This indicated that **8** could reduce the increase in mtROS induced by *P. acnes* stimulation in THP-1 cells. Moreover, Mito-TEMPO, a mitochondrial ROS scavenger, effectively re-

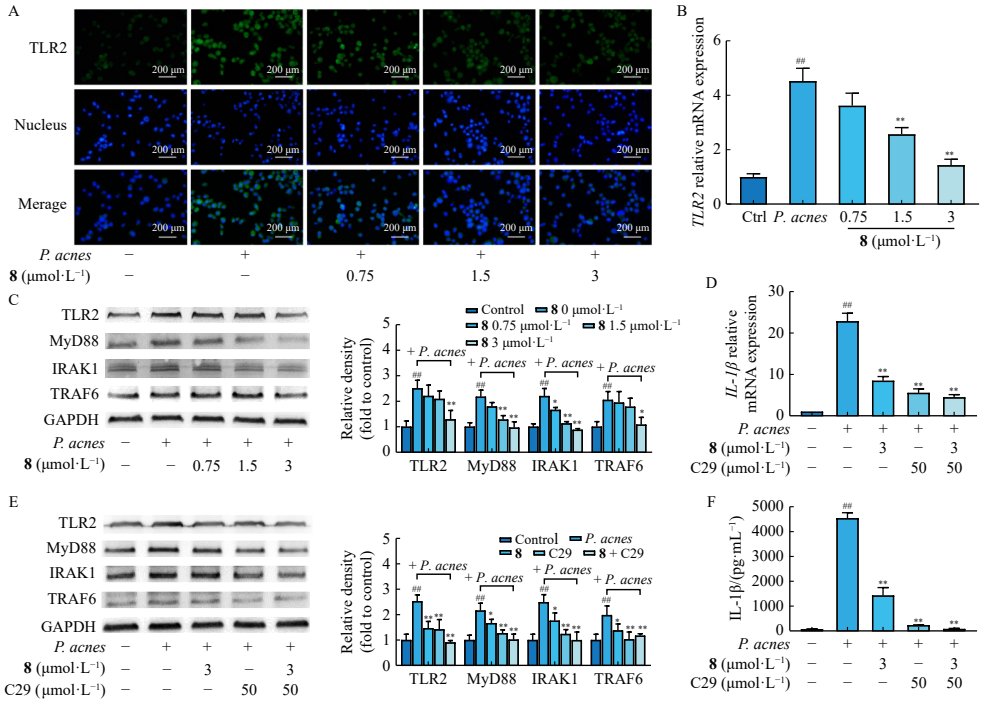

Fig. 5 Compound **8** attenuated inflammatory effects by inhibiting TLR signaling pathway in *P. acnes*-induced THP-1 cells. (A) The expression of TLR2 was visualized by immunofluorescence assay (scale bar = 50 μm). THP-1 cells were pretreated with **8** (3 μmol·L^{-1}) and/or C29 (50 μmol·L^{-1}) for 4 h prior to *P. acnes* stimulation. (B) The mRNA expression of *TLR2* was measured by real-time qRT-PCR and normalized using *GAPDH* as a reference gene. The cells were exposed to various concentrations of **8** for 24 h. (C) Representative immunoblots showing the effects of **8** on TLR2, MyD88, IRAK1 and TRAF6. THP-1 cells were treated with various concentrations of **8** for 24 h, and the expressions of indicated proteins were measured by Western blotting. (D) The expression of *IL-1β* mRNA after treated with **8**, C29 and **8** + C29 were determined by qRT-PCR. (E) Representative immunoblots showing the effects of **8**, C29 and **8** + C29, on TLR2, MyD88, IRAK1 and TRAF6. THP-1 cells were treated with various concentrations of **8** for 4 h, and the expressions of indicated proteins were measured by Western blotting. (F) The expression of IL-1β after treated with **8**, C29 and **8** + C29 were determined by ELISA. The results were expressed as means ± SD (n = 3). $^{\#\#}P < 0.01$ *vs* Control; $^{*}P < 0.05$, $^{**}P < 0.01$ *vs* Model.

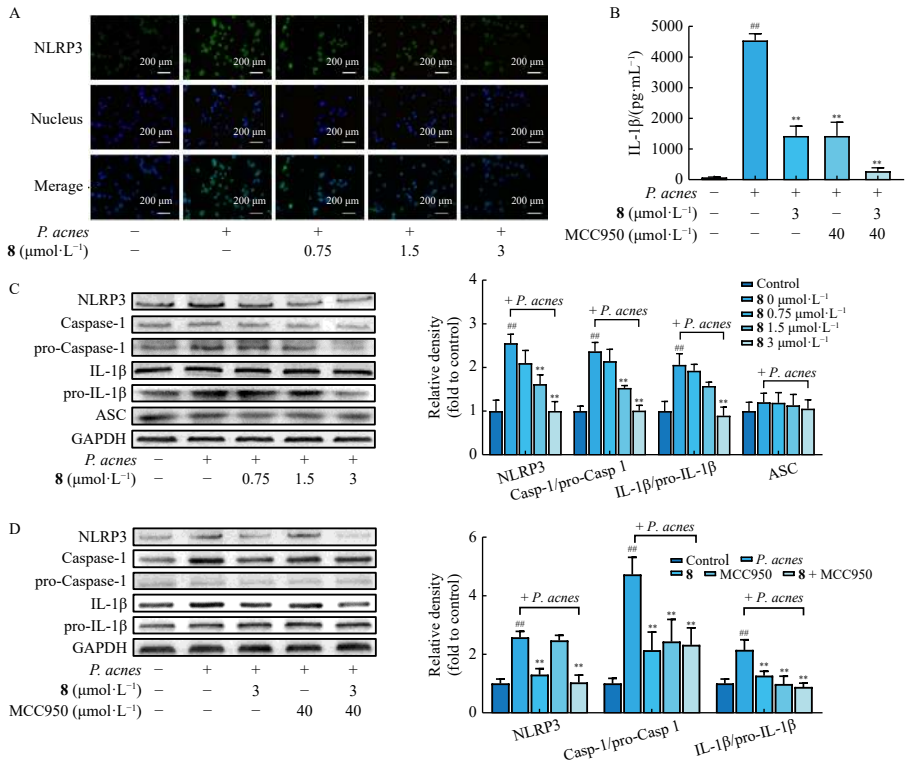

Fig. 6 Compound **8** suppressed *P. acnes*-induced NLRP3 inflammasome activation by ameliorating the level of mtROS. THP-1 cells were pre-treated with different concentrations of **8** for 4 h, followed by *P. acnes* stimulation for 1 h. (A) The localization and expression of NLRP3 was visualized by immunofluorescence assay. (B) The expressions of IL-1β after treated with **8**, MCC950 and **8** + MCC950, respectively, and were determined by ELISA. (C) Representative immunoblots showing the expression level of NLRP3, pro-caspase-1, caspase-1 (p20), pro-IL-1β, IL-1β and ASC after treated with **8**. THP-1 cells were pre-treated with different concentrations of **8** for 24 h, followed by *P. acnes* stimulation for 1 h, and the expressions of indicated proteins were measured by Western blotting. (D) Representative immunoblots showing the expression level of NLRP3, pro-caspase-1, caspase-1 (p20), pro-IL-1β, IL-1β and ASC of after treated with **8**, MCC950 and **8** + MCC950, respectively. THP-1 cells were pre-treated with different concentrations of **8** for 24 h, followed by *P. acnes* stimulation for 1 h, and the expressions of indicated proteins were measured by Western blotting. The results were expressed as means ± SD compared with GAPDH in the cytoplasm in the nucleus of three independent experiments. $^{\#\#}P < 0.01$ *vs* Control; $^{**}P < 0.01$ *vs* Model.

duced mtROS production induced by *P. acnes* stimulation (Fig. 7B). These results confirmed that **8** could decrease mtROS release in THP-1 cells upon *P. acnes* stimulation. Furthermore, ELISA assay results showed that Mito-TEMPO inhibited IL-1β secretion induced by *P. acnes* stimulation (Fig. 7B), indicating a correlation between mtROS production and IL-1β secretion. Considering the relationship between **8**'s inhibitory effects on IL-1β secretion and its suppression of mtROS, it is hypothesized that **8** may inhibit NLRP3 inflammasome activation by reducing mtROS production. To investigate whether **8**'s inhibitory effects on mtROS influence NLRP3 inflammasome activation, the impact of Mito-TEMPO on key activation-related proteins of NLRP3 inflammasomes was examined. Results showed that Mito-TEMPO could suppress the increase in protein expression of Caspase 1/pro-Caspase 1 and IL-1β/pro-IL-1β (Figs. 7C and 7D) induced by *P. acnes* stimulation. However, Mito-TEMPO showed minimal impact on NLRP3 protein expression (Fig. 7B), indicating that mtROS did not affect the initiation step of NLRP3 inflammasome activation but influenced inflammasome assembly. In conclusion, **8** can inhibit NLRP3 inflammasome activation by suppressing inflammasome assembly mediated by mtROS production in *P. acnes*-stimulated THP-1 cells, thereby leading to the suppression of IL-1β maturation and secretion.

Compounds **5**–**12** share similar structural frameworks, yet demonstrate notable differences in anti-inflammatory activity. Therefore, utilizing computer-aided drug design for structural-activity relationship analysis of this compound class provides advantages for further development and optimization of anti-inflammatory agents. 3D-QSAR incorporates molecular three-dimensional structural information for QSAR studies, providing a method to indirectly reflect the characteristics of non-bonding interactions between drug molecules and biological macromolecules. In comparison to 2D-QSAR, this approach offers clearer physical significance and more comprehensive informational content [31].

Accordingly, 3D-QSAR models were applied to perform comparative molecular field analysis (CoMFA) and comparative molecular similarity indices analysis (CoMSIA) on the aforementioned eight compounds, employing partial least squares (PLS) method to establish statistically significant CoMFA and CoMSIA models, with pIC_{50} values as the dependent variable and CoMFA and CoMSIA descriptors as the independent variables [32]. In the PLS analysis employing cross-validation method, the optimal number of components (ONC) and cross-validation correlation coefficient (Q^2) were determined using leave-one-out (LOO) approach. Subsequently, non-cross-validation method was employed to obtain standard error of estimation (SEE), Fischer test (F) value, and square of the non-cross-validation correlation coefficient (R^2), which were utilized to evaluate the predictive capability and stability of the models. The relevant statistical parameters obtained from PLS analysis of CoMFA and CoMSIA models are depicted in Table S1.

In conjunction with the most potent compound **8**, systematic analyses of CoMFA and CoMSIA contour maps were performed, as shown in Figs. S35–S36. Analysis of these steric contour maps (Figs. S35A–S36A) reveals a large yellow area around C3 of **8**, indicating minimal steric hindrance in this region, which facilitates increased compound activity, consistent with the presence of a double bond at this position **8**. Additionally, a large green area near C-21 indicates significant steric hindrance at this position, which promotes enhanced activity, suggesting that introducing large groups at this site can increase drug activity. Electrostatic analysis reveals a large blue area near N-1, indicating that increasing the number of positively charged groups in this region enhances the anti-inflammatory activity of the compound (Fig. S36B). Based on the analysis of compound activity data, it is concluded that nitrone plays a crucial role in enhancing the activity of this compound class. Therefore, utilizing the 3D-QSAR model, the analysis of the structure-activity relationship was conducted of compounds **5**–**12**, providing valuable insights for the modification of drug groups and the screening of similar compounds with stronger activity in the future.

3. Experimental

3.1. General experimental procedures

Optical rotations were measured using a JASCO P-1020 polar-

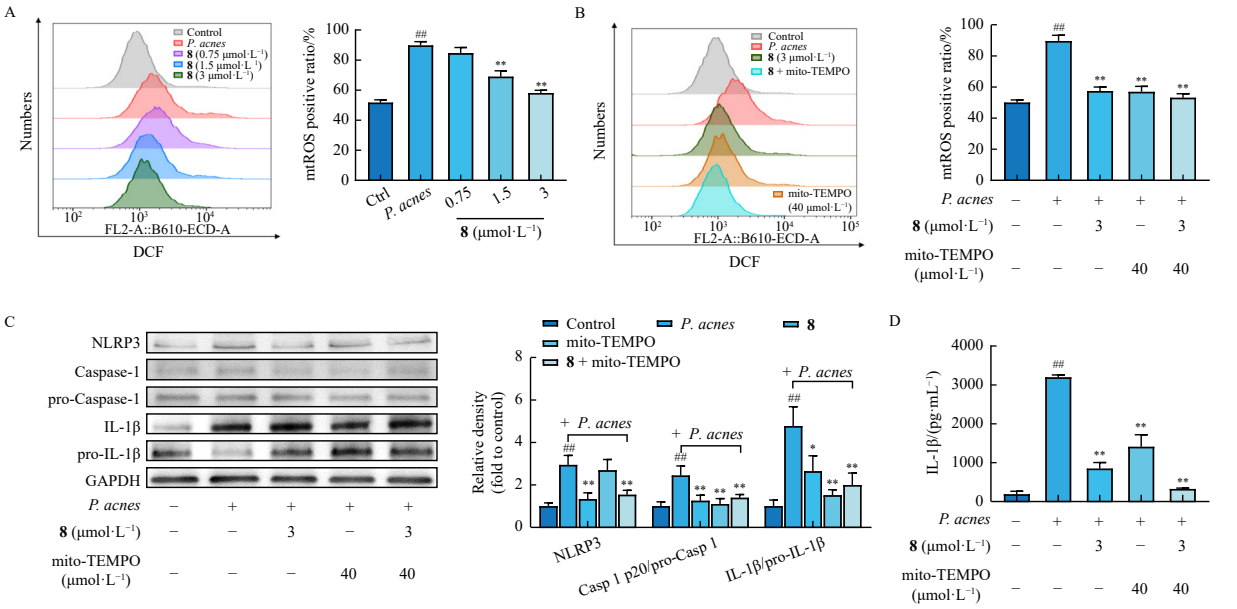

Fig. 7 Compound **8** suppressed *P. acnes*-induced NLRP3 inflammasome activation by ameliorating the level of mtROS. (A) Flow cytometry analysis of mitochondria-generated ROS by MitoSOX staining in THP-1 cells treated with or without **8** after *P. acnes* stimulation. THP-1 cells were pretreated with **8** (3 μmol·L^{-1}) and/or Mito-TEMPO (40 μmol·L^{-1}) for 4 h prior to *P. acnes* stimulation. (B) Mitochondria-generated ROS was analyzed by flow cytometry. (C) Representative immunoblots showing the expression level of pro-caspase-1, caspase-1, pro- IL-1β and IL-1β were measured by Western blotting. (J) The supernatant concentrations of IL-1β were determined by ELISA. THP-1 cells were pre-treated with different concentrations of **8** for 24 h, followed by *P. acnes* stimulation for 1 h. The results were expressed as means ± SD (n = 3). $^{\#\#}P < 0.01$ *vs* Control; $^{**}P < 0.01$ *vs* Model.

imeter (JASCO Corporation, Tokyo, Japan) in MeOH at 25 °C. UV spectra were recorded on a Shimadzu UV-1800 spectrophotometer (Shimadzu Corporation, Tokyo, Japan) in MeOH. ECD spectra were obtained by Chirascan circular dichroism spectrometers (Applied Photophysics Ltd., Leatherhead, UK). Both 1D and 2D NMR spectra were recorded on a Bruker AVIII-600 NMR spectrometer (Bruker Corporation, Rheinstetten, Germany), using TMS as an internal standard. HR-ESI-MS was carried out with an Agilent 6529B Q-TOF instrument (Agilent Technologies, Santa Clara, CA, USA). IR spectra, were tested on a Bruker FT-IR Tensor-27 (Bruker Optics, Ettlingen, Germany) and iCAN 9 infrared spectrophotometer using KBr disks. Column chromatography was performed on silica gel (200–300 mesh, Qingdao Marine Chemical Inc., Qingdao, China) and ODS (50 μm, YMC, Kyoto, Japan) on a Flash Chromatograph System (SepaBen machine, Santai Technologies, Changzhou, China). Preparative high-performance liquid chromatography [Pre-high performance liquid chromatography (HPLC)] was performed on a Shimadzu LC-20 system (Shimadzu, Tokyo, Japan) equipped with a Shim-pack RP-C_{18} column (20 mm × 250 mm i.d., 10 μm, Shimadzu, Tokyo, Japan) with a flow rate at 10 mL·min^{-1} at 25 °C. Human myeloid leukemia mononuclear cell (THP-1, Cell Bank of Type Culture Collection of Chinese Academy of Sciences, Shanghai, China) was cultured and passaged in RPMI 1640 medium containing 10% fetal bovine serum (KeyGEN Bio, Jiangsu, China) in a 5% CO_2 incubator at 37 °C. *P. acnes* (ATCC6919, Xiangfu Bio, Shanghai, China) was anaerobically cultured and passaged in beef medium containing beef granules (Rishui Bio, Qingdao, China) at 37 °C.

3.2. Fermentation, extraction, and isolation

The fungus was cultivated on potato dextrose agar (PDA) medium at 28 °C for 3 d. The grown strain was subsequently inoculated into a 250 mL Erlenmeyer flask containing 50 mL of potato dextrose broth (PDB). After 2 d of fermentation, the seed cultures were transferred to Erlenmeyer flasks (100 × 1000 mL), each containing 100 g of dry rice and 120 mL of distilled water, previously sterilized at 121 °C for 30 min. The flasks were incubated at room temperature for 28 d. Following incubation, the whole fermented rice medium was extracted three times using ethyl acetate (EtOAc), and the solvents were concentrated under reduced pressure to yield a crude extract (193.4 g). The crude extract was subjected to a macroporous resin column eluting by a gradient EtOH–H_2O (from 30%, 50%, 70% to 100% EtOH). The 50% fraction (33.6 g) was separated on a silica gel column eluting with a stepwise gradient of CH_2Cl_2–MeOH (from 25∶1 to 5∶1) to yield five subfractions (A–E). Fraction E (2.4 g) was further purified by an ODS column (MeCN–H_2O, 50∶50) and a semi-preparative HPLC eluting with 45% MeOH/H_2O to yield compounds **1** (8.6 mg, t_R 30.4 min), and **2** (17.4 mg, t_R 21.2 min). Fraction C (3.2 g) was further purified by an ODS column (MeCN–H_2O, 45∶55) and a semi-preparative HPLC eluting with 60% MeOH/H_2O to yield compounds **5** (12.3 mg, t_R 19.8 min), **3** (10.2 mg, t_R 15.6 min) and **4** (4.1 mg, t_R 16.3 min). Fraction B (3.6 g) was further purified by an ODS column (MeCN–H_2O, 65∶35) and a semi-preparative HPLC eluting with 55% ACN/H_2O to yield compounds **6** (17.6 mg, t_R 23.2 min), and **7** (13.4 mg, t_R 21.3 min). Fraction C (2.3 g) was further purified by an ODS column (MeCN–H_2O, 35∶65) and a semi-preparative HPLC eluting with 60% MeOH/H_2O to yield compound **8** (12.5 mg, t_R 31.2 min). The subfraction A4 was further purified by a semi-preparative HPLC eluting with 75% MeOH/H_2O to yield compounds **9** (12.3 mg, t_R 21.2 min), and **10** (10.1 mg, t_R 20.6 min). The subfraction A2 was further purified by a semi-preparative HPLC eluting with 65% MeOH/H_2O to yield **11** (7.3 mg, t_R 15.3 min), and **12** (7.6 mg, t_R 18.4 min).

Apertryptanthrin D (**1**): block crystal; $[\alpha]_D^{25}$ 28.0 (*c* 0.1, DMF); IR ν_{max} 3412, 2965, 1692, 1543, 1491 cm^{-1}; UV (MeOH) λ_{max} (log ε) 202 (4.53), 259 (3.61), 284 (3.90) nm; ECD (2.00 mmol·L^{-1}, MeOH) λ_{max} ($\Delta\varepsilon$) 217 (4.39), 240 (−1.86) nm; ^{1}H and ^{13}C NMR data, see Table 1; HR-ESI-MS: *m/z* 483.1659 $[M + H]^+$ (Calcd. for $C_{27}H_{23}N_4O_5$, 483.1663).

Crystal data for **1**: $C_{27}H_{22}N_4O_5$, *Mr*: 482.48, unit cell dimensions *a* = 5.9535 (3) Å, *b* = 12.4620 (6) Å, *c* = 28.9933 (15) Å, α= 90°, β = 90°, γ = 90°, *Z* = 4, volume = 2151.09 (19) Å^3, density (calculated) = 1.490 Mg·m^{-3}, μ = 0.865 mm^{-1}, F(000) = 1008.0, crystal size = 0.17 × 0.12 × 0.11 mm^3, radiation: Cu Kα (λ = 1.541 78), 2Θ range for data collection: 6.096 to 136.686°, index ranges: −7 ≤ h ≤ 7, −14 ≤ k ≤ 15, −33 ≤ l ≤ 34, reflections collected: 40178, independent reflections: 3732 [R_{int} = 0.0745, R_{sigma} = 0.0557], final *R* indexes [$I \geq 2\sigma(I)$]: R_1 = 0.0788, wR_2 = 0.1256, final *R* indexes [all data]: R_1 = 0.1083, wR_2 = 0.1369, largest diff. peak/hole = 0.25/−0.28 e·Å^{-3}, flack parameter = 0.10 (10).

Gartryprostatin D (**5**): block crystal; $[\alpha]_D^{25}$ −157.4 (*c* 0.1, MeOH); IR ν_{max} 3498, 2980, 1689, 1418, 1072 cm^{-1}; UV (MeOH) λ_{max} (log ε) 237 (4.16), 288 (3.64), 338 (3.50) nm; ECD (2.00 mmol·L^{-1}, MeOH) λ_{max} ($\Delta\varepsilon$) 226 (−4.68), 241 (−2.26) nm, 257 (−4.94); ^{1}H and ^{13}C NMR data, see Table 1; HR-ESI-MS: *m/z* 518.2263 $[M + Na]^+$ (Calcd. for $C_{26}H_{31}N_3O_6Na$, 518.2262).

Crystal data for **5**: $C_{26}H_{31}N_3O_6$, *Mr*: 495.58, unit cell dimensions *a* = 18.0410 (9) Å, *b* = 7.5501 (4) Å, *c* = 18.5120 (9) Å, α = 90°, β = 100.144 (2)°, γ = 90°, *Z* = 2, volume = 2482.1 (2) Å^3, density (calculated) = 1.350 Mg·m^{-3}, μ = 0.797 mm^{-1}, F(000) = 1076.0, crystal size = 0.12 × 0.06 × 0.04 mm^3, radiation: Cu Kα (λ = 1.541 78), 2Θ range for data collection: 4.85 to 149.356°, index ranges: 22 ≤ h ≤ 22, −9 ≤ k ≤ 9, −23 ≤ l ≤ 23, reflections collected: 21417, independent reflections: 5001 [R_{int} = 0.0588, R_{sigma} = 0.0438], final *R* indexes [$I \geq 2\sigma(I)$]: R_1 = 0.0386, wR_2 = 0.1010, final *R* indexes [all data]: R_1 = 0.0409, wR_2 = 0.1030, largest diff. peak/hole = 0.61/−0.17 e·Å^{-3}, flack parameter = −0.07 (8).

Crystal data for **2**: $C_{27}H_{22}N_4O_6$, *Mr*: 498.48, unit cell dimensions *a* = 17.431 (4) Å, *b* = 15.015 (3) Å, *c* = 18.374 (4) Å, α = 90°, β = 117.704 (11)°, γ = 90°, *Z* = 2, volume = 4257.5 (15) Å^3, density (calculated) = 1.217 Mg·m^{-3}, μ = 0.736 mm^{-1}, F(000) = 1632.0, crystal size = 0.15 × 0.06 × 0.05 mm^3, radiation: Cu Kα (λ = 1.541 78), 2Θ range for data collection: 5.432 to 137.098°, index ranges: −21 ≤ h ≤ 20, −17 ≤ k ≤ 17, −21 ≤ l ≤ 22, reflections collected: 51158, independent reflections: 14529 [R_{int} = 0.0852, R_{sigma} = 0.0905], final *R* indexes [$I \geq 2\sigma(I)$]: R_1 = 0.0671, wR_2 = 0.1765, final *R* indexes [all data]: R_1 = 0.1070, wR_2 = 0.1987, largest diff. peak/hole = 0.36/−0.28 e·Å^{-3}, Flack parameter = 0.39 (12).

Crystal data for **4**: $C_{27}H_{22}N_4O_5$, *Mr*: 482.48, unit cell dimensions *a* = 29.484 (11) Å, *b* = 29.484 (11) Å, *c* = 6.651 (4) Å, α = 90°, β = 90°, γ = 90°, *Z* = 6, volume = 5007.2 (5) Å^3, density (calculated) = 0.960 Mg·m^{-3}, μ = 0.558 mm^{-1}, F(000) = 1512.0, crystal size = 0.08 × 0.03 × 0.02 mm^3, radiation: Cu Kα (λ = 1.541 78), 2Θ range for data collection: 3.460 to 137.304°, index ranges: −34 ≤ h ≤ 35, −34 ≤ k ≤ 35, −7 ≤ l ≤ 7, reflections collected: 132080, independent reflections: 6137 [R_{int} = 0.1357, R_{sigma} = 0.0513], final *R* indexes [$I \geq 2\sigma(I)$]: R_1 = 0.0724, wR_2 = 0.1963, final *R* indexes [all data]: R_1 = 0.0979, wR_2 = 0.2131, largest diff. peak/hole = 0.20/−0.22 e·Å^{-3}, flack parameter = 0.13 (13).

3.3. X-ray crystallographic analysis

Crystallographic data for four compounds were collected using a Bruker D8 Venture diffractometer equipped with Cu Kα radiation (λ = 1.541 78 Å). The crystals were maintained at 170.0 K during data collection. The structure was determined using the ShelXT structure solution program with Direct Methods and refined using the ShelXL refinement package with Least Squares minimisation. The crystallographic data has been deposited at the Cambridge Crystallographic Data Centre with CCDC numbers

2290030 (**1**), 2068589 (**2**), 2347756 (**4**), 2142403 (**5**).

3.4. Anti-inflammatory assays

The human monocyte cell line THP-1 (Cell Bank of China Science Academy, Shanghai, China) and *P. acnes* (ATCC6919, Xiangfu biotech, Shanghai, China) were utilized in anti-inflammatory experiments. The *P. acnes* in logarithmic growth phase was employed to induce inflammation in THP-1 cells. The MTT method determined the safe concentration of tested compounds for THP-1 cells. Additionally, anti-microbial assays were conducted to exclude false anti-inflammatory activity arising from the compounds' inhibition of *P. acnes*. The inhibitory effect of test compounds on IL-1β secretion by THP-1 cells was evaluated through ELISA [33]. Detailed experimental procedures are provided in the Supporting information. All experiments were conducted in three independent replicates.

3.5. Immunofluorescence assay

THP-1 cells were preincubated for 4 h with compound **8**, followed by 1 h incubation with *P. acnes* in 6-well plates. The cells were subsequently harvested and purified. The cells underwent treatment with 4% paraformaldehyde for 30 min, 0.3% Triton X-100 for 10 min, and blocking with 3% BSA for 1 h. The cells were then incubated overnight at 4 °C with antibodies targeting TLR2, NLRP3, and phosphorylated p65. Further treatment included FITC-labelled goat anti-rabbit IgG antibody (Beyotime, Shanghai, China) in darkness for 1 h on ice. The cells were resuspended in an anti-fluorescence quenching sealing solution containing DAPI (Beyotime, Shanghai, China). A portion of cells was mounted onto slides for examination and imaging using a confocal fluorescence microscope.

3.6. ROS assay

THP-1 cells were cultured with **8** on 6-well plates for 4 h, followed by stimulation with *P. acnes* for 1 h. The cells were harvested and incubated with 5 μmol·L^{-1} mitoSOX red mitochondrial superoxide indicator (Yeasen Biotech, Shanghai, China) at 37 °C for 10 min in darkness. The cells were subsequently rinsed with HBSS buffer preheated to 37 °C, and ROS production was quantified through flow cytometry analysis.

3.7. Construction of CoMFA and CoMSIA models

The experimental bioactivity IC_{50} values in micromolar units were converted to negative logarithmic values (–log IC_{50}) for QSAR modeling. Compound structures were designed using ChemDraw 16.0 and optimized in SYBYL X 2.0 using the Tripos force field until reaching convergence at 0.01 kcal·mol^{-1}. Gasteiger–Hückel method calculated partial atomic charges. The lowest energy conformation was identified through multisearch approach and reserved for alignment. Molecular alignment, essential for 3D-QSAR models, employed atom-by-atom fitting based on compound **8**, the most potent molecule. After establishing a common substructure, dominant conformations of the remaining seven compounds were superimposed. The 3D-QSAR model was developed using SYBYL X 2.0 software. CoMFA and CoMSIA methodologies generated descriptors by placing superimposed compounds in a 3D cubic lattice with 2 Å grid spacing. Using sp^3 hybrid carbon as probe atom, steric and electrostatic field energies were calculated at each lattice point using Lennard–Jones and Coulomb potentials, while hydrogen bond acceptor, donor, and hydrophobic field contributions were evaluated. Linear correlations between CoMFA/CoMSIA fields and biological activity were analyzed using PLS method.

4. Conclusions

In conclusion, two novel indole diketopiperazines, aspertryptanthrin D (**1**) and gartryprostatin D (**5**), were isolated from the marine-derived fungus *Aspergillus* sp. The structural analysis revealed that compounds **1**, **2**, and **5** possess a rare 16-membered phenylate ring framework and a distinctive 6/6/5/5/5/6/5 seven-ring skeleton, confirmed through X-ray diffraction analysis. The configurations of compounds **2**–**4** were subsequently reassessed through comparative analysis of experimental and calculated ECD spectra and single-crystal X-ray diffraction analysis. The research demonstrates that asperthrin A (**8**) exhibits inhibitory effects on NLRP3 inflammasome activation and acne inflammation through multiple mechanisms. These mechanisms encompass the downregulation of TLR2-mediated activation of the MyD88-dependent pathway, MAPK and NF-*κ*B signaling pathways, and the inhibition of mitochondrial ROS production (Fig. S34). The 3D-QSAR model analysis suggests that compound **8** harbors significant potential for enhanced anti-inflammatory activity through structural modification. These findings establish compound **8** as a promising candidate for acne treatment or as an anti-inflammatory and anti-acne cosmetic ingredient. Furthermore, this research advances the understanding and application of marine resources in therapeutic development.

Funding

This work was supported by the National Natural Science Foundation of China (Nos. 41876189 and 81703388) and the State Key Laboratory of Bioreactor Engineering and Shanghai Collaborative Innovation Center for Biomanufacturing Technology.

Availability of supporting information

Supporting information for this study can be obtained by contacting the corresponding authors *via* E-mail.

Declaration of competing interest

These authors have no conflict of interest to declare.

References

1 Heng AHS, Chew FT. Systematic review of the epidemiology of acne vulgaris. *Sci Rep*. 2020;10(1):5754. https://doi.org/10.1038/s41598-020-62715-3.
2 Singam V, Rastogi S, Patel KR, et al. The mental health burden in acne vulgaris and rosacea: an analysis of the US national inpatient sample. *Clin Exp Dermatol*. 2019;44(7):766-772. https://doi.org/10.1111/ced.13919.
3 Kanwar IL, Haider T, Kumari A, et al. Models for acne: a comprehensive study. *Drug Discov Ther*. 2018;12(6):329-340. https://doi.org/10.5582/ddt.2018.01079.
4 Kircik L. Advances in the understanding of the pathogenesis of inflammatory acne. *J Drugs Dermatol*. 2016;15(1):s7-s10.
5 Contassot E, French LE. New insights into acne pathogenesis: *Propionibacterium acnes* activates the inflammasome. *J Invest Dermatol*. 2014;134(2):310-313. https://doi.org/10.1038/jid.2013.505.
6 Mohsin N, Hernandez LE, Martin MR, et al. Acne treatment review and future perspectives. *Dermatol Ther*. 2022;35(9):e15719. https://doi.org/10.1111/dth.15719.
7 Luo Z, Yin F, Wang XB, et al. Progress in approved drugs from natural product resources. *Chin J Nat Med*. 2024, 22(3): 195-211. https://doi.org/10.1016/S1875-5364(24)60582-0.
8 Hong Q, Guo MM, Yang J, et al. Four previously undescribed diketopiperazines from marine fungus *Aspergillus puniceus* FAHY0085 and their effects on liver X receptor α. *Phytochemistry*. 2023;214:113816. https://doi.org/10.1016/j.phytochem.2023.113816.
9 Guo JC, Yang J, Wang P, et al. Anti-vibriosis bioactive molecules from Arctic *Penicillium* sp. Z2230. *Bioresour Bioprocess*. 2023;10(1):11. https://doi.org/10.1186/s40643-023-00628-5.
10 Ding Y, Jiang Y, Xu SJ, et al. Perpyrrospirone A, an unprecedented hirsutellone peroxide from the marine-derived *Penicillium citrinum*. *Chin Chem Lett*. 2023;34(2):107562. https://doi.org/10.1016/j.cclet.2022.05.076.
11 Yang J, Gong LZ, Guo MM, et al. Bioactive indole diketopiperazine alkaloids

from the marine endophytic fungus *Aspergillus* sp. YJ191021. *Mar Drugs*. 2021;19(3):157. https://doi.org/10.3390/md19030157.
12 He WW, Xu YC, Fu P, et al. Cytotoxic indolyl diketopiperazines from the *Aspergillus* sp. GZWMJZ-258, endophytic with the medicinal and edible plant *Garcinia multiflora*. *J Agric Food Chem*. 2019;67(38):10660-10666. https://doi.org/10.1021/acs.jafc.9b04254.
13 Lhamo S, Wang XB, Li TX, et al. Three unusual indole diketopiperazine alkaloids from a terrestrial-derived endophytic fungus, *Aspergillus* sp. *Tetrahedron Lett*. 2015;56(21):2823-2826. https://doi.org/10.1016/j.tetlet.2015.04.058.
14 Kato H, Yoshida T, Tokue T, et al. Notoamides A–D: prenylated indole alkaloids isolated from a marine-derived fungus, *Aspergillus* sp. *Angew Chem Int Ed*. 2007;46(13):2254-2256. https://doi.org/10.1002/anie.200604381.
15 Afiyatullov SS, Zhuravleva OI, Antonov AS, et al. Prenylated indole alkaloids from co-culture of marine-derived fungi *Aspergillus sulphureus* and *Isaria felina*. *J Antibiot*. 2018;71(10):846-853. https://doi.org/10.1038/s41429-018-0072-9.
16 Whyte AC, Gloer JB, Wicklow DT, et al. Sclerotiamide: a new member of the paraherquamide class with potent antiinsectan activity from the sclerotia of *Aspergillus sclerotiorum*. *J Nat Prod*. 1996;59(11):1093-1095. https://doi.org/10.1021/np960607m.
17 Tsukamoto S, Kato H, Samizo M, et al. Notoamides F–K, prenylated indole alkaloids isolated from a marine-derived *Aspergillus* sp. *J Nat Prod*. 2008;71(12):2064-2067. https://doi.org/10.1021/np800471y.
18 Tsukamoto S, Umaoka H, Yoshikawa K, et al. Notoamide O, a structurally unprecedented prenylated indole alkaloid, and notoamides P–R from a marine-derived fungus, *Aspergillus* sp. *J Nat Prod*. 2010;73(8):1438-1440. https://doi.org/10.1021/np1002498.
19 Sugimoto K, Sadahiro Y, Kagiyama I, et al. Isolation of amoenamide A and five antipodal prenylated alkaloids from *Aspergillus amoenus* NRRL 35600. *Tetrahedron Lett*. 2017;58(29):2797-2800. https://doi.org/10.1016/j.tetlet.2017.05.057.
20 Pretre V, Papadopoulos D, Regard J, et al. Interleukin-1 (IL-1) and the inflammasome in cancer. *Cytokine*. 2022;153:155850. https://doi.org/10.1016/j.cyto.2022.155850.
21 Kim J. Review of the innate immune response in acne vulgaris: activation of toll-like receptor 2 in acne triggers inflammatory cytokine responses. *Dermatol*. 2005;211(3):193-198. https://doi.org/10.1159/000087011.
22 Beylot C, Auffret N, Poli F, et al. *Propionibacterium acnes*: an update on its role in the pathogenesis of acne. *J Eur Acad Dermatol Venereol*. 2014;28(3):271-278. https://doi.org/10.1111/jdv.12224.
23 Gambero M, Teixeira D, Butin L, et al. *Propionibacterium acnes* induces an adjuvant effect in B-1 cells and affects their phagocyte differentiation *via* a TLR2-mediated mechanism. *Immunobiology*. 2016;221(9):1001-1011. https://doi.org/10.1016/j.imbio.2016.03.003.
24 Chiu A, Chon SY, Kimball AB. The response of skin disease to stress: changes in the severity of acne vulgaris as affected by examination stress. *Arch Dermatol*. 2003;139(7):897-900. https://doi.org/10.1001/archderm.139.7.897.
25 Fitzgerald KA, Kagan JC. Toll-like receptors and the control of immunity. *Cell*. 2020;180(6):1044-1066. https://doi.org/10.1016/j.cell.2020.02.041.
26 Chang L, Karin M. Mammalian MAP kinase signalling cascades. *Nature*. 2001;410(6824):37-40. https://doi.org/10.1038/35065000.
27 Barnabei L, Laplantine E, Mbongo W, et al. NF-κB: at the borders of autoimmunity and inflammation. *Front Immunol*. 2021;12:716469. https://doi.org/10.3389/fimmu.2021.716469.
28 Bauernfeind FG, Horvath G, Stutz A, et al. Cutting edge: NF-κB activating pattern recognition and cytokine receptors license NLRP3 inflammasome activation by regulating NLRP3 expression. *J Immunol*. 2009;183(2):787-791. https://doi.org/10.4049/jimmunol.0901363.
29 Kelley N, Jeltema D, Duan Y, et al. The NLRP3 inflammasome: an overview of mechanisms of activation and regulation. *Int J Mol Sci*. 2019;20(13):3328. https://doi.org/10.3390/ijms20133328.
30 Zhou RB, Yazdi AS, Menu P, et al. A role for mitochondria in NLRP3 inflammasome activation. *Nature*. 2011;469(7329):221-225. https://doi.org/10.1038/nature09663.
31 Wang YW, Guo YF, Qiang SJ, et al. 3D-QSAR, molecular docking, and MD simulations of anthraquinone derivatives as PGAM1 inhibitors. *Front Pharmacol*. 2021;12:764351. https://doi.org/10.3389/fphar.2021.764351.
32 Cramer RD, Patterson DE, Bunce JD. Comparative molecular field analysis (CoMFA). 1. Effect of shape on binding of steroids to carrier proteins. *J Am Chem Soc*. 1988;110(18):5959-5967. https://doi.org/10.1021/ja00226a005.
33 Guo M, An F, Yu H, et al. Comparative effects of schisandrin A, B, and C on *Propionibacterium acnes*-induced, NLRP3 inflammasome activation-mediated IL-1β secretion and pyroptosis. *Biomed Pharmacother*. 2017;96:129-136. https://doi.org/10.1016/j.biopha.2017.09.097.